

July 10, 2021

FUV Irradiation and the Heat Signature of Accretion in Protoplanetary Disk Atmospheres

Joan R. Najita¹ and Máté Ádámkóvics²

¹*National Optical Astronomical Observatory, 950 North Cherry Avenue, Tucson, AZ 85719
najita@noao.edu*

²*Astronomy Department, 501 Campbell Hall, University of California, Berkeley, CA 94720
mate@berkeley.edu*

ABSTRACT

Although stars accrete mass throughout the first few Myr of their lives, the physical mechanism that drives disk accretion in the T Tauri phase is uncertain, and diagnostics that probe the nature of disk accretion have been elusive, particularly in the planet formation region of the disk. Here we explore whether an accretion process such as the magnetorotational instability could be detected through its “heat signature”, the energy it deposits in the disk atmosphere. To examine this possibility, we investigate the impact of accretion-related mechanical heating and energetic stellar irradiation (FUV and X-rays) on the thermal-chemical properties of disk atmospheres at planet formation distances. We find that stellar FUV irradiation ($\text{Ly}\alpha$ and continuum), through its role in heating and photodissociation, affects much of the upper warm (400–2000 K) molecular layer of the atmosphere, and the properties of the layer are generally in good agreement with the observed molecular emission features of disks at UV, near-infrared, and mid-infrared wavelengths. At the same time, the effect of FUV irradiation is restricted to the upper molecular layer of the disk, even when irradiation by $\text{Ly}\alpha$ is included. The region immediately below the FUV-heated layer is potentially dominated by accretion-related mechanical heating. As cooler (90–400 K) CO, water, and other molecules are potential diagnostics of the mechanically-heated layer, emission line studies of these diagnostics might be used to search for evidence of the magnetorotational instability in action.

Subject headings: planetary systems: protoplanetary disks — accretion, accretion disks — astrochemistry

1. INTRODUCTION

The gas-rich disks that surround young stars at birth play a starring role in the build up of stellar masses and in the origin of planets. Mass is transported through the disk onto the star, and

the gas and dust in the disk is available for planet formation. Emission lines from disk atmospheres offer clues to the dynamical state of the gas (e.g., probing disk rotation, turbulent line broadening), its chemical transformation (e.g., synthesis of organic molecules), and the processes that determine the thermal properties of the atmosphere (Rab et al. 2016; Carmona 2010; Najita et al. 2007.)

The thermal structure of the disk affects both its chemistry and observational signatures. Observations reveal that the gaseous atmosphere in the planet formation region of the disk reaches higher temperatures than the dust, a result of poor gas-grain thermal coupling at the low density conditions in the upper disk atmosphere (Kamp & van Zadelhoff 2001; Glassgold & Najita 2001). UV-fluorescent H₂ emission lines indicate the presence of hot H₂ (1500–3500 K) within 1 AU of the star (Herczeg et al. 2004; Schindhelm et al. 2012). Near-infrared (2–5 μm) emission lines from simple molecules (CO, OH, water) that arise primarily from within 0.3 AU also reveal that the gaseous atmosphere reaches temperatures of 1500 – 3000 K (e.g., Carr et al. 1993, 2004; Najita et al. 2003; Salyk et al. 2009; Doppmann et al. 2011). Similarly, mid-infrared emission from water, OH and other molecules (10–20 μm) within ~ 1 AU has a characteristic temperature of ~ 500 – 1000 K (Carr & Najita 2011; Salyk et al. 2011a). These temperatures are higher than the dust temperature at the same disk radii (e.g., D’Alessio et al. 2006).

Various mechanisms have been proposed to account for the elevated gas temperatures, including irradiation by stellar X-ray and FUV photons (Glassgold et al. 2004; Kamp & Dullemond 2004; Gorti & Hollenbach 2008; Nomura et al. 2007; Ercolano et al. 2009; Woitke et al. 2009; Woods & Willacy 2009; Heinzeller et al. 2011; Walsh et al. 2012; Akimkin et al. 2013; Du & Bergin 2009). The stellar FUV emission from accreting T Tauri stars is powered by stellar accretion, whereas their X-ray emission is powered by stellar activity. The disk can also be heated by accretion-related mechanical heating, either from a wind blowing over the disk or through the dissipation of gravitational energy as material accretes through the disk (Glassgold et al. 2004).

Historically, thermal-chemical studies of disk atmospheres have focused primarily on the role of heating by FUV continuum photons through the photoelectric effect on grains and PAHs or H₂ photodissociation (e.g., Kamp & van Zadelhoff 2001; Jonkheid et al. 2004). Photoelectric heating is an attractive mechanism given the higher luminosity of stellar FUV emission ($L_{\text{FUV}} \simeq 10^{31} \text{ erg s}^{-1}$; e.g., Yang et al. 2012) compared to stellar X-rays ($L_X \simeq 10^{30} \text{ erg s}^{-1}$; e.g., Wolk et al. 2005) and its natural ability to concentrate energy deposition at the top of the atmosphere. However, efficient photoelectric heating requires abundant grains in the disk atmosphere, in potential conflict with the short settling times of grains (e.g., Chiang & Goldreich 1997; D’Alessio et al. 1999).

The suspicion that disk atmospheres are significantly depleted in grains, and the consequent reduction in photoelectric heating efficiency, led Glassgold et al. (2004) to explore X-ray irradiation and mechanical heating as alternative processes. Significant grain settling in T Tauri disks, by factors of $10^{-3} - 10^{-2}$ relative to interstellar conditions, is indeed inferred observationally (Furlan et al. 2005). However, the recent recognition that molecules become the primary FUV absorbers at low grain abundances, and that the resulting photochemical heating is an efficient way to heat

disk atmospheres (Bethell & Bergin 2009; Glassgold & Najita 2015; Najita et al. 2009) returns FUV to prominence in heating the disk surface (Ádámkóvics et al. 2014, 2016; hereafter AGN14 and ANG16, respectively).

Nevertheless, the role of mechanical heating in disk atmospheres remains of interest, not only to understand the thermal structure of disk atmospheres, but also as a potential probe of the mechanism that drives disk accretion (e.g., Glassgold et al. 2004; Bai & Goodman 2009). Despite clear evidence for continued accretion onto stellar surfaces throughout the first few Myr of a star’s life, the physical process that redistributes angular momentum in T Tauri disks (and thereby allows accretion to occur) remains frustratingly unknown (see Turner et al. 2014 for a review). Thus it is of interest to explore whether the accretion process might reveal clues about its nature through its energy dissipation in the disk atmosphere.

While all accretion processes release gravitational energy, the different candidate processes differ in where they deposit their accretion energy (Turner et al. 2014). The magnetorotational instability (MRI; Balbus & Hawley 1992) dissipates accretion energy higher in the disk, on average, than the height at which accretion occurs, a result of the buoyancy of the magnetic field (Hirose & Turner 2011). In addition, the active region of the disk at planet formation distances of $\sim 1\text{--}10$ AU is restricted to a surface layer, because deeper layers are insufficiently ionized to participate in the instability (Gammie 1996). As a result, the energy dissipation is further concentrated toward the disk surface.

The volumetric heating rate due to the MRI can be quite large, with potential observable consequences. Hirose & Turner (2011) estimate a dissipation rate in the disk atmosphere equivalent to $\alpha_h \sim 1$, where α_h is the accretion-related mechanical heating parameter, defined in Glassgold et al. (2004) as $\Gamma_{\text{acc}} = 9/4\alpha_h\rho c^2\Omega$ where ρ is the local mass density, c is the isothermal sound speed, and Ω is the angular rotation speed of the disk. In comparison, the value of the viscosity parameter for accretion α , when vertically averaged over the column density of the *entire* disk, is much smaller, $\sim 10^{-2}$, based on T Tauri accretion rates (Hartmann et al. 1998). Recent theoretical studies find that the MRI may be weak or inoperative in the planet formation region, creating a potential bottleneck for disk accretion, which may be solved by magnetically-driven winds (e.g., Bai & Stone 2013; Kunz & Lesur 2013; Lesur et al. 2014; Gressel et al. 2015). Developing observational probes of MRI activity in the planet formation region of the disk may allow us to observationally verify or challenge this scenario.

Here we explore possible observational signatures of mechanical heating in disk atmospheres in the context of irradiation heating. We make use of our recently updated thermal-chemical model of a disk atmosphere that is heated by stellar FUV and X-rays as well as accretion-related mechanical heating (ANG16). We previously used the model to study the impact of stellar Ly α irradiation on the disk atmosphere at small radii (~ 0.3 AU), implementing the Ly α radiative transfer in a simple approach that includes scattering by HI and absorption by molecules and dust.

With this approach, we found that the increased heating by Ly α produced a new component of

the model atmosphere close to the star: hot (1500–2500 K) molecular gas (ANG16). The properties of the hot component (temperature, column density, emitting area) may help to explain the origin of the UV fluorescent H₂ emission that is detected commonly from classical T Tauri stars (Herczeg et al. 2004; Schindhelm et al. 2012). The observed UV H₂ emission is well explained by strong dipole electronic transitions pumped by Ly α from excited vibrational levels of H₂. While the vibrational levels have been assumed to be populated non-thermally, by UV and X-ray irradiation (Nomura et al. 2007), our results suggest that the H₂ vibrational levels can be excited through a thermal pathway.

Here we use the same model to search for regions of the disk atmosphere that are dominated by accretion-related mechanical heating and to identify potential observational diagnostics of those regions. We also compare the warm columns predicted by our model with the properties of observational diagnostics of disk atmospheres at UV, near-infrared, and mid-infrared wavelengths. In the following sections we describe the thermal-chemical model (§2) and its properties (§3) and discuss its ability to account for known observational diagnostics of disks and whether accretion-related mechanical heating generates a detectable heat signature (§4). The representative results and figures presented in §3 focus on the results at 0.5 AU, which are relevant to the mid-infrared diagnostics. These are supplemented in Appendix A with additional figures and discussion that describe the model results at larger radii. Related results at smaller radii were discussed previously in ANG16. Appendix B describes in greater detail the observed properties of disk atmospheres against which our model results are compared.

2. THERMAL-CHEMICAL MODEL

We use a thermal-chemical model of an X-ray and FUV irradiated disk that was most recently described in ANG16. The model, which builds on earlier work described in Glassgold et al. (2004, 2009) and Ádámkóvics et al. (2011), assumes a static disk density and dust temperature structure (D’Alessio et al. 1999) along with the stellar and disk parameters from ANG16, which are listed in Table 1. As in ANG16, the adopted dust properties reflect the assumption that grains have grown and settled quickly to the midplane, leaving behind a reduced population of small grains in the disk atmosphere. The grain size parameter $a_g = 0.7\mu\text{m}$ corresponds to a reduction in the grain surface area by a factor of 20 compared to interstellar conditions and a dust surface area per hydrogen nucleus that is $S_d \approx 8 \times 10^{-23} \text{ cm}^2$.

With these assumptions, we solve the thermal and chemical rate equations to determine the gas temperature and species abundances. The calculations include the FUV photochemistry of water and OH (AGN14) as well as additional abundant molecules and atoms (ANG16). We adopt the photochemical heating rates detailed in Glassgold & Najita (2015; hereafter GN15). Most notably, as in ANG16, we consider the radiative transfer and photochemistry of Ly α separately from the FUV continuum.

Table 1. Reference Model Parameters

Parameter	Symbol	Value
Stellar mass	M_*	$0.5 M_\odot$
Stellar radius	R_*	$2 R_\odot$
Stellar temperature	T_*	4000 K
Disk mass	M_D	$0.005 M_\odot$
Disk accretion rate	\dot{M}	$10^{-8} M_\odot \text{ yr}^{-1}$
Dust to gas ratio	ρ_d/ρ_g	0.01
Dust grain size	a_g	$0.7 \mu\text{m}$
Dust extinction	Q_{ext}	1.0
X-ray temperature	T_X	1 keV
X-ray luminosity	L_X	$2 \times 10^{30} \text{ erg s}^{-1}$
FUV continuum luminosity ^a	L_{FUV}	$1 \times 10^{31} \text{ erg s}^{-1}$
Ly α /FUV continuum ^b	η	3
Accretion heating	α_h	0.5

^aThe FUV continuum luminosity is integrated from 1100–2000 Å and excludes Ly α , so that it is smaller than the value used in AGN14.

^bThe ratio of the unattenuated downward Ly α photon number flux to the radially-propagating FUV continuum number flux in 1200-1700Å band.

^cThe total disk column density varies with disk radius as $\Sigma \approx 100(r/\text{AU})^{-1} \text{ g cm}^{-2}$.

The stellar FUV emission from accreting T Tauri stars has contributions from both the continuum and the Ly α line, although it is the latter that dominates the luminosity (Herczeg et al. 2004). As it propagates radially away from the star, the FUV continuum is attenuated by dust and molecules in the disk atmosphere. The attenuation by an absorber a depends on the line-of-sight column of the absorber from the star through the atmosphere $N_{a,\text{los}}$. To specify the line-of-sight columns in our model, we calculate the ratio of the column densities of hydrogen nuclei along the line-of-sight and vertically in the D’Alessio atmosphere $N_{\text{H,los}}/N_{\text{H}}$. The line-of-sight column of the absorber is then approximated as $N_a(N_{\text{H,los}}/N_{\text{H}})$, where N_a is the vertical column density of the absorber.

Studies that reconstruct the stellar Ly α emission find that it accounts for $\sim 90\%$ of the FUV emission from accreting T Tauri stars. Ly α photons leaving the star are scattered in an atomic wind before reaching the disk, with a large fraction of the Ly α scattered away from the disk. As a result, the Ly α flux is comparable to the flux of FUV continuum photons at the transition from atomic to molecular conditions in the disk atmosphere (Schindhelm et al. 2012; Bethell & Bergin 2011, hereafter BB11). Because the scattered Ly α photons reaching the disk travel more directly downward, their penetration into the disk is increased compared to that of FUV continuum photons, which propagate at an oblique angle into the disk (BB11).

Once in the disk atmosphere, the radiative transfer of Ly α is complex. In contrast to the radiative transfer of the FUV continuum, which is governed primarily by absorption due to dust or molecules, Ly α photons are also scattered by atomic hydrogen, which is abundant at the top of the disk atmosphere. As a result of the increased scattering, Ly α has a longer path length through the absorptive medium and is efficiently attenuated in the upper molecular region of the atmosphere (BB11, ANG16).

Here, as in ANG16, we adopt a schematic treatment of Ly α radiative transfer (scattering and absorption) based on the detailed work in the above studies. For simplicity, we assume that Ly α photons reaching the disk propagate directly downward in contrast to the radially propagating FUV continuum photons. We also set the ratio of the number flux of Ly α photons to the number flux of FUV continuum photons in the 1200–1700Å band to be $\eta = 3$ at the top of the atmosphere in our reference model.

Because Ly α photons are scattered by H I in the disk atmosphere, the photons have a larger effective path length through the atmosphere and a greater likelihood of being absorbed by dust and molecules. We treat this effect in a simple, approximate way. As described in ANG16, in order to traverse a grid cell of length ℓ that has a scattering mean free path of $\ell_s = 1/n_s\sigma_s$, where n_s and σ_s are the number density and cross section of scatterers, a Ly α photon will take approximately τ_s^2 steps, where $\tau_s = n_s\sigma_s\ell = \ell/\ell_s$. As a result, the photon travels a distance of approximately $\ell_{\text{eff}} = \tau_s^2\ell_s = \tau_s\ell$ through the absorbing medium. Because of the longer path length, the effective optical depth for absorption is approximately

$$\tau_{\text{eff}} \equiv n_a\sigma_a\ell_{\text{eff}} = \tau_a\tau_s, \tag{1}$$

where n_a and σ_a are the number density and absorption cross of absorbers, and τ_a is the absorption optical depth. The increased path length leads to increased Ly α (intensity and) absorption, which both attenuates the Ly α and enhances its photochemical and photoelectric heating.

In our earlier study focusing on the impact of Ly α irradiation at small disk radii, we found that the increased heating in that region of the disk produced a new component of the disk atmosphere: hot (1500–2500 K) molecular gas that may account for the UV fluorescent H₂ emission that is detected commonly from classical T Tauri stars. Because the treatment of Ly α scattering is approximate, our results should be considered illustrative rather than quantitative. An improved treatment that includes scattering effects in a more realistic way is needed to understand the effect of Ly α on the detailed properties of the atmosphere.

Our model also includes self-shielding in the 900–1000Å band. The opacity in the band is dominated by H₂, CO, N₂, and C, with H₂, CO, and N₂ self- and mutually shielding one another as well as other species. To include these processes, we use the H₂ shielding function from Draine & Bertoldi (1996), tabulations of CO shielding from Visser et al. (2009), and N₂ shielding from Li et al. (2013), following the prescription described in ANG16.

Water vapor, an important source of FUV opacity, can freeze out onto cold grains at dust temperatures of 100–125 K (e.g., Woods & Willacy 2009; Woitke et al. 2009; Meijerink et al. 2009; Heinzeller et al. 2011) At radial distances within a few AU of the star, the grains in the disk atmosphere are warm enough that an insignificant amount of water is condensed onto their surface, while at larger radial distances freezeout becomes more of a concern. We consider the freezeout of water onto grain surfaces by calculating the rate of adsorption and balance it with the rate of water removal from grains via thermal- and photo-desorption (Fraser et al. 2001; Öberg et al. 2009).

The rate of water adsorption onto grains is determined by the rate at which molecules strike grains, $R_{\text{ads}} = n(\text{H}_2\text{O})\bar{v}(\text{H}_2\text{O})S_d$, where $\bar{v}(\text{H}_2\text{O}) = \sqrt{8kT/18\pi m_H}$ is the mean thermal velocity of the water molecules and $n(\text{H}_2\text{O})$ is their number density. We assume unit sticking probability once a water molecule strikes a grain. Thermal desorption is included as a zeroth order process based on the experimental results of Fraser et al. (2001) and is implemented with a treatment similar to that of Visser et al. (2011). Photodesorption is determined by the local FUV photon number flux and a temperature-dependent photodesorption efficiency given by Öberg et al. (2009). Water molecules desorb intact 70% of the time and otherwise as OH + H.

In addition to the approximate Ly α radiative transfer described above, there are several other shortcomings of the model. One shortcoming is that hydrostatic equilibrium is not enforced, i.e., when we calculate the gas temperature, we do not adjust the assumed density structure, that of the D’Alessio et al. (1999) model, to maintain pressure balance. Because the gas temperature exceeds the dust temperature in the upper atmosphere, we overestimate the density there. We also assume that the dust abundance and size distribution are the same at all heights and radii in the atmosphere. Transport of material (radial or vertical) is not considered, and we assume that the chemical timescales are rapid enough that abundances and thermal rates are determined by local

conditions.

To explore the impact of not enforcing hydrostatic equilibrium, we carried out a simple experiment in which we adjusted the density profile of the atmosphere to approximate hydrostatic equilibrium and then recalculated its thermal-chemical structure. We found that the lack of explicit hydrostatic equilibrium did not greatly affect the properties (temperature, abundances) of the atmosphere. The recalculated molecular abundances and temperatures were within a factor of 2 and within 10%, respectively, of their original values in the region where the molecules produce most of their emission. We estimate that the errors in temperature and abundances that result from the lack of hydrostatic equilibrium do not exceed those derived from uncertainties in other model properties such as the extent of grain growth, and the luminosity and propagation of the scattered Ly α component of the UV field.

3. Results

At high altitude, the gaseous disk atmosphere is hot (~ 5000 K) and in atomic form (Figures 1, 2, top panels, solid lines). In our reference model, in which $\alpha_h = 0.5$, mechanical heating is the primary heating mechanism at the top of the atmosphere, although FUV heating is also important (Figure 1, middle panel). Because molecules are absent in this region of the atmosphere, photochemical heating is unimportant, and the FUV heats through its interaction with grains via the photoelectric effect.

At intermediate altitudes (strawberry-colored regions), simple molecules (e.g., H₂, OH, H₂O) are abundant, although much of the hydrogen is in atomic form (Figure 2, middle panel). Ly α photons are scattered by the HI in this layer, and the OH and H₂O absorb FUV photons (both Ly α and continuum; Figure 1, bottom panel). The resulting photochemical heating dominates the heating (Figure 1, middle panel), and the atmosphere is very warm as a result ($\sim 800 - 1000$ K) from 0.5–2 AU (Figure 1, top panel and Appendix A, Figure 7). As they deposit their energy, the Ly α flux is significantly attenuated through the layer and the FUV continuum plummets (Figure 1, bottom panel).

At lower altitudes, immediately below the FUV-heated layer (chocolate-shaded region), mechanical heating dominates (Figure 1, middle panel), and H₂ is the dominant form of hydrogen (Figure 2, middle panel). Lacking significant FUV heating and subject to stronger dust-gas collisional cooling because of the higher density, the gas in this region of the atmosphere is cooler than in the intermediate layer but nevertheless warmer than the dust in the same region of the atmosphere (Figure 1, top panel, dotted line). While Ly α is greatly attenuated through the FUV-heated layer, the photon flux that survives into the layer below is significant ($\sim 10^{12}$ photons cm⁻²), and Ly α dominates the FUV field at depth (Figure 1, bottom panel; BB11). Water declines in abundance in the chocolate-shaded layer as a consequence of continued photodissociation and the declining gas temperature; the latter reduces the neutral formation rate of water (see also AGN14).

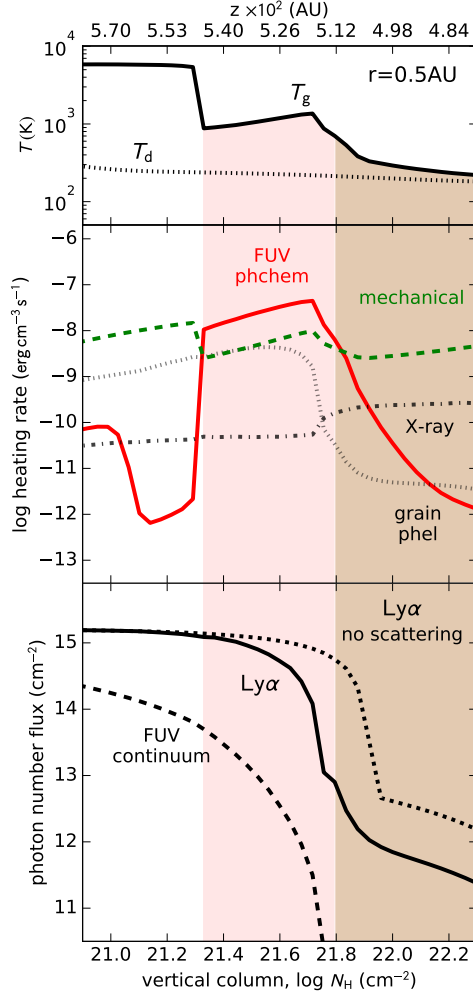


Fig. 1.— Vertical profiles of gas and dust temperatures (top panel, solid and dotted lines, respectively), heating rates (middle panel), and FUV radiation fields (bottom panel) at $r = 0.5$ AU in our reference model. FUV photochemical heating (red solid line) dominates in the warm upper molecular layer of the disk (strawberry shading) where the FUV continuum and $\text{Ly}\alpha$ are absorbed. Mechanical heating (green dashed line) dominates above and below this region. X-ray (dash-dotted line) and grain photoelectric heating (dotted line) are shown for comparison. The FUV continuum and $\text{Ly}\alpha$ are strongly attenuated in the photochemically-heated layer.

Figure 3 shows the impact of $\text{Ly}\alpha$ irradiation on the thermal-chemical properties of the atmosphere. If the $\text{Ly}\alpha$ component of the FUV field were not present, the molecular portion of the atmosphere would be cooler (top panel, dashed line). Water would be more abundant and atomic H less abundant in both the strawberry and chocolate layers at 0.5 AU to 2 AU (bottom panel, blue and black dashed lines, respectively; see also Appendix A, Figure 9). OH, a dissociation product of water, would also be much less abundant at all radii (bottom panel, green dashed line).

Figure 4 shows the impact of mechanical heating on the atmosphere. Mechanical heating affects

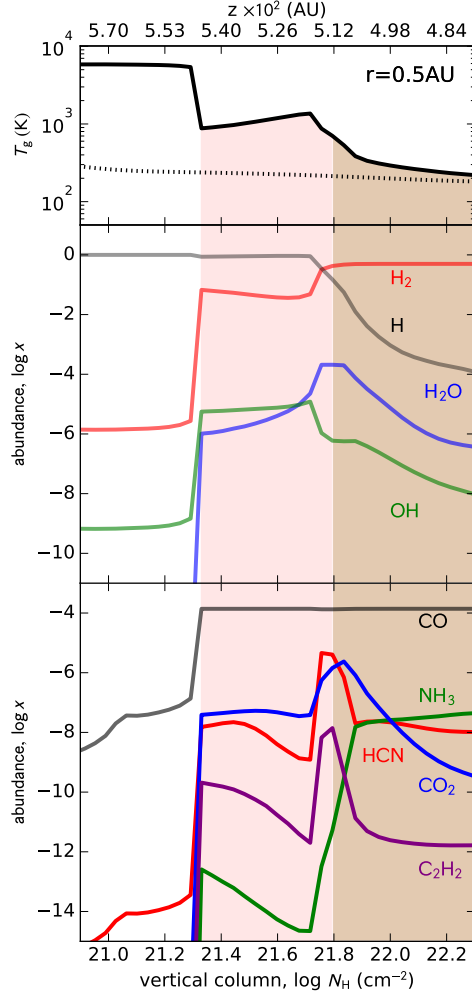


Fig. 2.— Vertical profiles of temperatures (top panel) and abundances (middle and bottom panels) at $r = 0.5$ AU in our reference model. The warm upper layer where FUV heating dominates (strawberry shading) is rich in molecular species that are commonly detected from T Tauri disks. The cooler mechanically heated layer (chocolate shading) lies below.

the structure above and below the FUV-heated layer (Fig. 1). At high altitudes, the transition from the hot atomic layer to the FUV-heated layer occurs higher in the atmosphere when mechanical heating is absent (dashed line) than when it is present (solid line).

The reason for this difference is that the transition from atomic to molecular conditions is regulated by the balance between H_2 formation on grains and its collisional destruction by atomic hydrogen ($\text{H}_2 + \text{H} \rightarrow 3\text{H}$). The destruction pathway is critically sensitive to temperature, with the rate coefficient declining by 15 orders of magnitude between 3000 and 1000 K (Palla et al. 1983). The feedback between increased molecular cooling and decreased H_2 destruction leads to the sharp transition from atomic to molecular conditions (AGN14). If mechanical heating increases

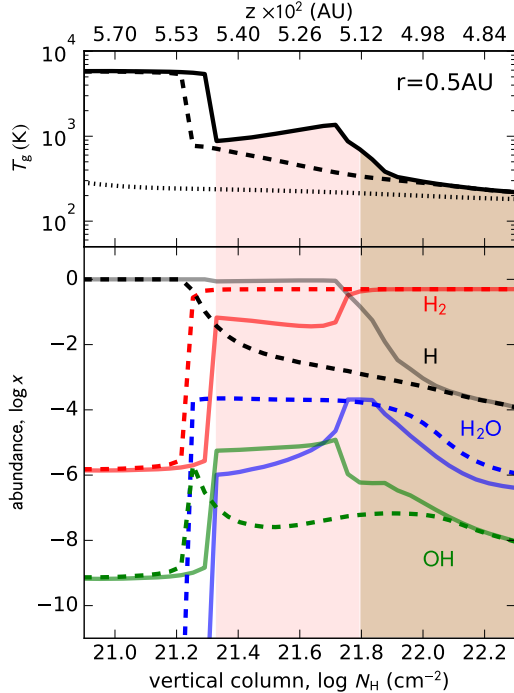


Fig. 3.— Vertical profiles of gas temperatures (top panel) and molecular abundances (bottom panel) with and without Ly α irradiation (solid and dashed lines respectively) at $r = 0.5$ AU. When Ly α is not present, the molecular portion of the atmosphere is cooler, and the molecular transition occurs higher in the atmosphere. When present, Ly α dissociates H $_2$ O and enhances the OH abundance in both the FUV-heated (strawberry shading) and mechanically-heated (chocolate shading) layers.

in the region of the transition from atomic to molecular conditions, H $_2$ destruction increases rapidly and the layer becomes atomic, pushing the transition deeper towards the midplane. Conversely, when mechanical heating is reduced, the tipping point of the transition is reached higher in the atmosphere.

Deeper in the disk, below the FUV-heated layer, the gas temperature at all radii (0.5 AU to 10 AU) is cooler without mechanical heating than when mechanical heating is present. As a result, the column density of warm gas is enhanced when mechanical heating is present. Figure 5 shows that the gas column density in the disk atmosphere in the temperature range 90–400 K is large, $\gtrsim 10^{22}$ cm $^{-2}$, and 4–10 times larger beyond 1 AU when mechanical heating is present (solid green line) than when it is absent (dashed green line). At the smaller radii ($\lesssim 1$ AU), mechanical heating enhances the column density of gas at higher temperatures. At 0.5 AU the column density of gas in the 200–400 K region is 4 times larger with mechanical heating than without. To exclude any warm molecular gas that is present deep in the atmosphere, near the (unobservable) disk midplane, the column densities shown in the figure are restricted to the surface $N_H = 10^{23}$ cm $^{-2}$ of the disk.

CO is an attractive potential diagnostic of the mechanically heated layer. Relatively insensitive

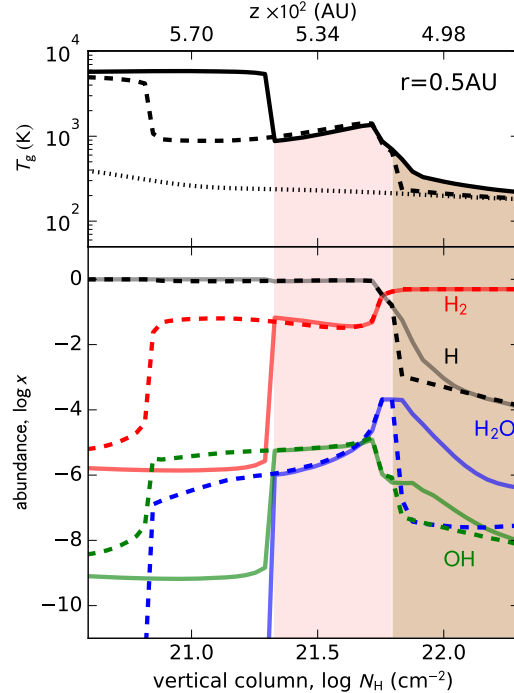


Fig. 4.— Vertical profiles of gas temperatures (top) and molecular abundances (bottom) with and without mechanical heating (solid and dashed lines, respectively) at $r = 0.5$ AU. When mechanical heating is reduced, the molecular transition occurs higher in the atmosphere and the temperature is reduced in the molecular region below the FUV-heated layer.

to other factors (e.g., the intensity of $\text{Ly}\alpha$ flux in the layer, or the location of the snow line), CO is reliably present in the molecular atmosphere at high abundance in and below the FUV-heated layer ($x_{\text{CO}} \sim 10^{-4}$; Figure 2; see also Appendix A, Figure 8). At 2–10 AU, the CO column density in the temperature range 90–400 K is $\gtrsim 10^{18} \text{ cm}^{-2}$ when mechanical heating is present and ~ 4 –10 times lower when it is absent.

Other potential diagnostics of the mechanically heated layer depend more sensitively on other factors. For example, the abundance of water in the layer depends on both the strength of mechanical heating and the flux of $\text{Ly}\alpha$. Mechanical heating raises the gas temperature, an effect that tends to increase the abundance of water, which depends sensitively on temperature (e.g., Glassgold et al. 2009). Conversely, $\text{Ly}\alpha$ photodissociates water and reduces its abundance.

As a result of these two effects, the abundance of water in the mechanically heated layer varies with radius. At 0.5 AU, the $\text{Ly}\alpha$ flux is reduced significantly, by ~ 1000 , through the FUV-heated layer and the mechanically heated layer is warmed to > 250 K. Because the neutral synthesis pathway for water is active in this temperature range, the layer contains a significant column of warm water. At larger radii, the $\text{Ly}\alpha$ flux is reduced by a smaller factor through the FUV-heated

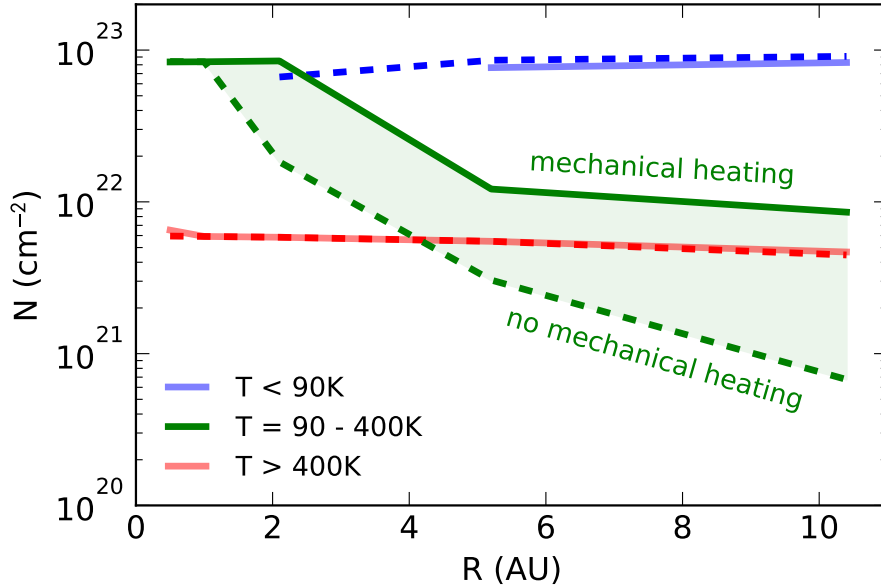


Fig. 5.— Gas column densities in the disk atmosphere in several temperature ranges as a function of disk radius with (solid lines) and without (dashed lines) mechanical heating. Mechanical heating enhances the column density in the 90–400 K temperature range.

layer (by ~ 100 at 1 AU; Appendix A, Figure 7), the mechanically-heated layer is cooler than 250 K, and little water is present in that layer as a result (Appendix A, Figure 9).

The upper molecular region of the reference model (strawberry-shaded region in the figures) captures the general properties of the molecular emission observed from the inner regions of T Tauri disks. Figure 6 compares the warm molecular column densities in the disk atmosphere model with the warm molecular emission columns inferred from spectroscopy. The shaded regions indicate the general properties of the molecular emission detected by *Spitzer* from T Tauri disks (OH, H₂O, HCN, CO₂, C₂H₂, and upper limits on NH₃). The properties are derived from simple slab fits to the emission, parameterized by molecular column density, emission temperature, and emitting area πR_e^2 (Carr & Najita 2011, 2008; Salyk et al. 2011a).

In Figure 6, the height of the shaded region indicates the typical range of observed molecular emission columns, and the shaded region extends out to typical values of R_e . The heavy solid lines show, as a function of disk radius, the warm columns from the reference model within the temperature range reported for the emission. The relevant temperature range is indicated in the legend in each panel.

Figure 6 also shows the results described previously for H₂ and CO (ANG16) using the same approach as for the *Spitzer* diagnostics described above. The large columns of hot H₂ ($\log N_{\text{H}_2} \sim 19$ at 1500–3500 K) produced within 0.3 AU in the model are comparable to the properties inferred

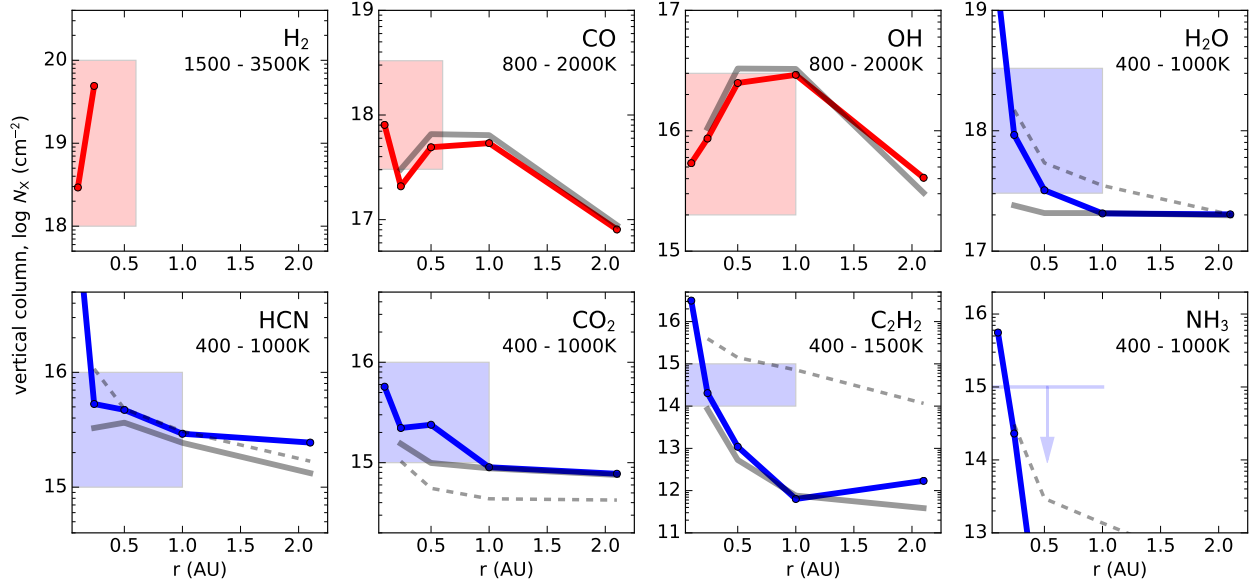


Fig. 6.— Warm gas column densities in the reference model within the temperature range inferred for the observed diagnostics as a function of disk radius (colored solid lines) compared with the range of column densities and emitting radii inferred observationally for the diagnostic (shaded region) in the same temperature range. The shaded region extends out to the inferred value of R_e (see text for details). The observational upper limit on the column density of warm NH_3 is indicated by the downward arrow. The model results without mechanical heating ($\alpha_h = 0.01$; solid gray lines) and without Ly α (dashed gray lines) are shown for comparison. The reference model is in good agreement with the observations for most species.

for the hot H_2 that produces the UV fluorescent H_2 emission from T Tauri stars. H_2 temperatures and column densities of $T_{\text{H}_2} = 2500 \pm 1000$ K and $\log N_{\text{H}_2} = 19 \pm 1$ are inferred from the analysis of UV H_2 emission from T Tauri stars (Schindhelm et al. 2012; Herczeg et al. 2004). The resolved UV H_2 line profiles of normal (non-transition) T Tauri stars (FWHM $\sim 50\text{--}70$ km s^{-1} ; France et al. 2012) suggest that most of the emission arises from within ~ 0.7 AU.

The CO rovibrational emission from T Tauri stars has line widths comparable to those of the UV H_2 emission, indicating that it also arises from primarily within 0.7 AU. Typical (deprojected) CO emission columns and temperatures are $\log N_{\text{CO}} = 17.5 - 18.5$ and 900–1600 K, respectively (Salyk et al. 2011a,b; Najita et al. 2003; Banzatti & Pontoppidan 2015). These properties are similar to the hot columns of CO found in the reference model. In general, the molecular properties of the reference model are in good agreement with those of the observed molecular emission from T Tauri disks at UV, NIR, and MIR wavelengths.

The relative roles of FUV and mechanical heating in the reference model are also illustrated in Figure 6. The results for models with no mechanical heating ($\alpha_h = 0.01$) and no Ly α are shown as light solid and light dashed lines, respectively. Comparing these results with those of the reference model shows that the column densities of hot H_2 , CO, and warm OH are similar whether mechanical

heating is present (heavy solid line) or not (light solid line), i.e., these quantities are dominated by FUV heating. There is no dashed line in these panels because mechanical heating alone (in the absence of FUV) does not create a warm enough atmosphere to contribute molecular emission in the temperature ranges indicated.

Mechanical heating does help to enhance the column density of water in the 400–1000 K temperature range, whereas FUV heating alone falls short of the observed warm water column density, in part because the FUV dissociates water. The column density of warm CO₂ is also best matched in the model with both mechanical heating and Ly α . Although C₂H₂ is underproduced in the reference model, it is fairly abundant when Ly α is weak. Perhaps a model with more modest Ly α irradiation beyond the hot H₂ emitting region may be able to produce hot H₂ and CO close to the star, while also retaining a reasonable column density of C₂H₂ at larger radii. Models with detailed Ly α radiative transfer would be valuable in exploring this possibility.

4. Discussion

We find that stellar FUV irradiation, through its role in heating and photodissociation, affects much of the disk atmosphere that produces the well-known molecular emission diagnostics of inner disks. In particular, Ly α photons, with their distinctive radiative transfer, have a significant impact on the thermal-chemical structure of the upper atmosphere. In ANG16 we found that our simple prescription for Ly α radiative transfer, which includes scattering by HI and absorption by molecules and dust, can account for the large column densities of hot UV fluorescent H₂ and rovibrational CO emission detected from T Tauri disks at small radii ($\lesssim 0.5$ AU), properties of long standing that have been otherwise difficult to explain. Here we find that the FUV-irradiated layer of the atmosphere at larger radii (out to ~ 1 AU) can also account for the *Spitzer* OH, H₂O, HCN, and CO₂ emission that is commonly detected from T Tauri disks (Fig. 6). As described in §3, while the observations are best fit with a model that includes both UV irradiation (Ly α and continuum) and mechanical heating, the UV (and Ly α in particular) does much of the heavy lifting.

4.1. OH as a Probe of Ly α Irradiation

Ly α irradiation also produces abundant OH in the planet formation region, with the OH/H₂O column density ratio in the atmosphere in good agreement with observations. Because the upper disk atmosphere has a significant atomic component, strong scattering by HI at the disk surface enhances Ly α absorption by molecules and dust. The Ly α component deposits energy deeper in the atmosphere than the FUV continuum (Figure 1) enhancing the temperature of the upper molecular layer which rises to $\gtrsim 1000$ K (Figure 2). OH is abundant throughout this region, because the FUV energy is deposited through dissociation of water, producing OH. FUV irradiation thus produces a layered atmosphere of very warm (> 1000 K) OH with a column density of $\sim 3 \times 10^{16}$ cm⁻² at

0.5 AU, overlying cooler (1000-500 K) water, with a column density $\sim 5 \times 10^{17} \text{ cm}^{-2}$. Thus, when Ly α scattering is included, the upper atmosphere is hotter and OH is more abundant than when scattering is ignored.

These results differ from those of AGN14, in which we treated the radiative transfer of Ly α in the same fashion as the FUV continuum, i.e., as pure attenuation. In that study, we found a shallower photochemically heated layer. As a result, the warm column ratio of OH/H₂O was $\sim 1/300$ at ~ 1 AU rather than the ratio of $\sim 1/10$ found here for the same total stellar (Ly α + continuum) FUV luminosity. Column density ratios in this range are similar to the OH/water emission column density ratio inferred from *Spitzer* spectra of T Tauri stars (Salyk et al. 2011a; Carr & Najita 2008). *Spitzer* observations indicate an OH emission column density $\sim 0.01 - 0.1$ that of water, assuming that the two diagnostics have similar emitting areas, with the OH having a higher average temperature than the water as well, as in the model results.

One limitation of our model is that the Ly α radiative transfer is treated very approximately. For example, we assume that at all disk radii the number flux of downward-propagating Ly α photons at the top of the atmosphere is a constant value of $\eta = 3$ times the number flux of FUV continuum photons, following the results of BB11. The BB11 calculations are themselves approximate. While they include HI scattering and dust absorption of Ly α , they do not treat the synthesis of FUV-absorbing molecules such as OH and H₂O. The latter shortcoming can be addressed with calculations that integrate sophisticated Ly α radiative transfer in a disk atmosphere (e.g., BB11) with detailed chemistry (e.g., as in Du & Bergin 2014).

Observations can also help to constrain the role of Ly α in heating disk atmospheres. Because Ly α has such a strong impact on the OH column density, high resolution spectroscopy of the OH emission detected by *Spitzer* can measure the OH column density and temperature as a function of radius, for comparison with the results obtained here. The comparison will lend insight into whether the treatment of Ly α employed here is approximately correct and where it fails.

4.2. Molecular Probes of Mechanical Heating

While stellar FUV irradiation has a significant impact on the upper disk atmosphere, its thermal effect is restricted to the disk surface even when irradiation by Ly α is included. With the impact of FUV irradiation thus restricted, mechanical heating has the opportunity to imprint a signature on the thermal-chemical properties of the layer below it. Detailed attention to the properties of this region of the atmosphere may open opportunities to detect its effects.

Our results suggest CO as a potential diagnostic of this region. Because its abundance is relatively insensitive to UV irradiation and the thermal structure of the atmosphere, the column density of warm CO may serve as a signature of an atmosphere warmed by mechanical heating. At disk radii 1–10 AU, the CO column density in the temperature range 90–400 K is $\gtrsim 10^{18} \text{ cm}^{-2}$ and 4–10 times higher when mechanical heating is present than when it is absent (§3). CO in the 100–

500 K range is detectable in the FIR and submillimeter. For example, Meeus et al. (2013) detected CO emission in this temperature range from T Tauri stars and Herbig AeBe stars using *Herschel* PACS. Among the T Tauri stars, the observations were only sensitive to bright CO emission from energetic sources with evidence for winds and outflows (e.g., DG Tau, AS205A). More sensitive measurements are needed to detect warm CO emission from less active, more typical T Tauri stars.

Molecules more sensitive to UV irradiation are also potential tracers of the mechanically-heated layer, although they are trickier to employ. The abundances in the mechanically-heated layer of molecules that are dissociated by Ly α (Bergin et al. 2003) depend on the details of Ly α propagation through the FUV-heated layer. In addition, molecules like water are sensitive to mechanical heating in two ways, firstly because the abundance of water is sensitive to temperature (the synthesis of water through the neutral chemistry pathway weakens considerably below ~ 250 K) and secondly through the excitation of the water transitions themselves. As a result, in the inner disk (< 1 AU), the strength of water emission from the mechanically-heated layer depends on both Ly α propagation through the FUV-heated layer as well as mechanical heating. If we can better understand Ly α propagation, “lukewarm” (200-500 K) water emission, detectable at mid-infrared wavelengths, is a potentially useful diagnostic of a mechanically heated layer. At 0.5 AU, the column density of lukewarm water is $\sim 1 \times 10^{17}$ cm $^{-2}$ in the reference model and more than 100 times smaller when mechanical heating is absent.

Our results expand on and endorse those of Hirose & Turner (2011). They previously showed that while stellar irradiation dominates the heating in the surface layer of the disk at 1 AU, turbulent dissipation of magnetic and kinetic energy can dominate the heating in the layer immediately below it (their Figure 1). By treating in detail the properties of the gaseous atmosphere, including the role of FUV irradiation, we are able to estimate the thermal-chemical properties of the layer in which mechanical heating may produce a distinctive observational signature.

4.3. The Heat Signature of Accretion in Context

Observational signatures of mechanical heating in inner disks (< 10 AU) would complement the ongoing search for evidence of the MRI in outer protoplanetary disks through the turbulent motions that they are expected to generate. Non-thermal line broadening, at the level of $\sim 50\%$ of the sound speed that is measured in spatially resolved line emission ~ 200 AU away from the star, had been inferred and interpreted as evidence for turbulent line broadening generated by the MRI in outer disks (HD163296—Hughes et al. 2011; DM Tau—Guilloteau et al. 2012). More recent, higher resolution observations with ALMA of HD163296 favor lower levels of non-thermal broadening, at the level of only $\lesssim 5\%$ (Flaherty et al. 2015) or $\sim 10\%$ (de Gregorio-Monsalvo et al. 2013) of the sound speed. Larger non-thermal line widths, 20–40% of the sound speed, have been reported for the TW Hya disk beyond 40 AU (Teague et al. 2016).

In contrast to the outer disk, the inner, planet formation region of the disk is much less

favorable to the MRI. The high disk column density at few AU distances ($\sim 2000 \text{ g cm}^{-2}$ at 1 AU in the minimum mass solar nebula) shields the midplane from ionizing radiation, and the high midplane density enhances recombination. The resulting low ionization fraction deep in the disk produces a midplane “dead zone” in which the MRI is not expected to operate (Gammie 1996). As a result, any accretion is expected to be restricted to the disk surface.

Recent work on the impact of non-ideal MHD effects on the MRI suggest that ambipolar diffusion and the Hall effect suppress the MRI in the planet formation region (1–10 AU) even in the surface layers of the disk; magneto-thermal disk winds, launched from the externally heated and ionized disk surface, have emerged as an alternative angular momentum removal mechanism at planet formation distances (Bai & Stone 2013; Kunz & Lesur 2013; Gressel et al. 2015; Bai et al. 2016). The wind mass loss rates are thought to be large, a considerable fraction of the wind-driven disk accretion rate (Bai et al. 2016). Bai et al. (2016) suggest that observational evidence for such a massive wind might be found in the low-velocity blueshifted forbidden line emission from T Tauri stars (e.g., OI 6300Å; Simon et al. 2016), although the thermal and dynamical properties of the wind are still uncertain enough that detailed predictions have not been made for comparison with observations.

Given the uncertain state of the theoretical predictions for angular momentum transport through disks or via disk winds, it seems prudent to look for ways to determine *observationally* whether the MRI is active or not at planet formation distances. One approach is to look for chemical evidence of turbulent motions produced by the MRI. If gas is transported (vertically or radially) in turbulent eddies quickly enough, it may be unable to equilibrate chemically to the local conditions (temperature, density, irradiation field), and a chemically distinctive signature of turbulent transport may be observable. This approach is challenging in inner disk atmospheres, because the chemical timescale is short or comparable to the dynamical time. In our models, the chemical timescale at 1 AU is much shorter than 1 year for most species, similar to the results found by other investigators (e.g., Thi & Bik 2005), which suggests a limited role for dynamical mixing in determining the abundances of these species (cf. Heinzeller et al. 2011).

Another possibility is to search for evidence of non-thermal line broadening, as in the millimeter studies, but on small (spatially unresolved) scales. Evidence for suprathreshold line broadening at very small disk radii ($< 0.3 \text{ AU}$) has been reported in systems with high disk accretion rates based on $2.3\mu\text{m}$ CO overtone emission (e.g., Carr et al. 2004; Doppmann et al. 2009; Najita et al. 1996, 2009). These studies show that the closely-spaced lines near the $v=2-0$ CO bandhead can be used to probe the local line broadening, even with spatially unresolved data. When the lines at the bandhead are optically thick, the varying line overlap as a function of inter-line separation produced by local line broadening imprints a distinctive shape on the CO bandhead, and the local line broadening can be recovered with spectral synthesis modeling. Evidence for non-thermal line broadening from CO overtone emission is not surprising. The temperature of the gas that produces the CO overtone emission is high enough ($> 1000 \text{ K}$) to thermally ionize alkali elements, and non-ideal MHD effects are expected to be weak, and the MRI active, as a result.

Extending these measurements to the larger disk radii where a dead zone is expected (1–10 AU) requires diagnostics that probe cooler gas at larger radii and also offer sets of closely spaced lines with a range of line spacings. Infrared transitions of water may be appropriate (Carr et al. 2004), as T Tauri stars commonly show a rich spectrum of water emission in the mid-infrared (Carr & Najita 2008, 2011; Pontoppidan et al. 2010). This approach has yet to be attempted.

Given the above challenges, searching for the “heat signature” of turbulent dissipation is a third, potentially promising option that we have explored here. To summarize, in our study of the effect of accretion related mechanical heating and energetic stellar irradiation (FUV and X-rays) on the thermal-chemical properties of disk atmospheres, we find that the effects of FUV heating, by both continuum and Ly α , are restricted to the upper molecular layer of the disk. The properties of the warm molecular layer, derived in the model, are generally in good agreement with the observed properties of disks inferred from spectroscopy at UV, NIR, and MIR wavelengths.

With FUV heating and photodissociation restricted to the disk surface layer, the way is open for the MRI to potentially signal its presence through accretion-related mechanical heating in the layer below. Warm CO, water, and other molecules are potential diagnostics of this region of the disk. To obtain robust predictions of signposts of mechanical heating, detailed work is needed on Ly α propagation through disk atmospheres and the chemistry of the region below the FUV-heated layer.

Some of our conclusions may be altered by the presence of magneto-thermal disk winds, which have been proposed as an alternative mechanism for disk angular momentum transport (Bai & Stone 2016, 2013; Lesur et al. 2014; Gressel et al. 2015). If disk winds are massive, they can affect the predicted properties of disk atmospheres, e.g., by attenuating stellar FUV and X-rays before they reach the disk. A wind that is primarily atomic and entrains small dust grains as it leaves the disk atmosphere will scatter stellar Ly α photons and attenuate FUV photons. If considerably less Ly α and FUV continuum reaches the disk as a result, the good agreement between the properties of disk atmosphere and the molecular emission properties of disks described here would be compromised. The reduction in irradiation heating would increase the need for other heating sources such as mechanical heating. Future studies of irradiated atmospheres that include an intervening disk wind component would therefore lend insights into the properties of winds and the role of mechanical heating in disks.

We thank the referee for valuable comments. This work was performed in part at the Aspen Center for Physics, which is supported by National Science Foundation grant PHY-1066293. It also benefitted from the National Science Foundation Grant No. NSF PHY11-25915 to the Kavli Institute for Theoretical Physics. JN acknowledges the stimulating research environment supported by NASA Agreement No. NNX15AD94G to the “Earths in Other Solar Systems” program. M acknowledges support by NASA XRP grant NNX15AE24G.

Appendix A. Supplementary Figures

The comparison in Figure 6 of the model properties of the warm molecular atmosphere with the molecular emission properties observed from disks requires calculations at radii beyond 0.5 AU. In this Appendix, we present supporting model results at 1 AU and 2 AU (Figs. 7–10) that extend the results shown in Figures 1–4 to larger radii.

Figure 7 shows the gas and dust temperatures, heating rates, and FUV irradiation fields at 0.5 AU, 1 AU, and 2 AU in the reference model. While the $1/r^2$ dilution of the stellar FUV and Ly α radiation field affects the peak temperature reached in the FUV-heated (strawberry-shaded) region, the general characteristics of the layered structure at 0.5 AU (§3) are similar at the larger radii. FUV photochemical heating still dominates in the warm upper molecular layer. As the heating rates decrease with disk radius and decreasing local volumetric density, the cooling rates (not shown) also decrease with radius, and a similar temperature structure is maintained out to 2 AU (see also ANG16 and AGN14).

Figure 8 shows the molecular abundances as a function of vertical column at 0.5 AU, 1 AU, and 2 AU. The FUV-heated layer (strawberry shading) always has a significant, although not fully, molecular component as measured by $x(\text{H}_2)$. The freeze-out of water beyond 1 AU has a significant impact on the molecular abundances; e.g., the gas phase abundances of water and OH are reduced in the mechanically-heated layer (chocolate shading). Two additional figures, which show the model results with and without Ly α irradiation (Fig. 9) and mechanical heating (Fig. 10), illustrate how the differences found at 0.5 AU (§3) are qualitatively similar out to 2 AU.

Appendix B. Properties of Observed Molecular Diagnostics

As discussed in §3, the range of values shown in Figure 6 for the observed temperature, column density, and emitting area for each molecular diagnostic reflect the range of values measured from source to source and/or the uncertainty in the reported values. The observations underlying the molecular emission properties summarized in the figure are described in greater detail below. While the figure attempts to make a general comparison between the model results and the emission properties of CTTS as a group, more detailed comparisons could be made for individual sources, by comparing the warm columns reported for an individual source with the results of models tailored to its properties (e.g., its FUV continuum, Ly α , and X-ray luminosities, extent of grain settling, etc).

Simple slab models with a single temperature and column density and a given emitting area are often employed to characterize the molecular emission. In general, the reported properties, derived assuming LTE, reproduce the observed spectra fairly well. The good agreement is surprising in some cases given the potential for non-LTE level populations (H₂O—Meijerink et al. 2009; HCN—Bruderer et al. 2015; CO₂—Bosman et al. 2017); sub-thermal populations may bias the LTE fit to lower temperatures. Because real disks are expected to show variations in temperature and density as a function of disk radius and height, the fit parameters are average values over the disk emitting volume. The choice of features to include in a slab model also introduces systematic differences in the results between studies.

UV Fluorescent H₂

Populating the excited vibrational levels of H₂ that can be fluoresced by Ly α photons requires temperatures ~ 2500 K, if the excitation is thermal (Herczeg et al. 2004; Schindhelm et al. 2012). In their study of H₂ emission from TW Hya, Herczeg et al. (2004) found an H₂ excitation temperature of 2500 K (+700 K/-500 K) and an H₂ column density of $\log(N_{\text{H}_2}/\text{cm}^{-2}) = 18.5 (+1.2/-0.8)$, and constrained the emission to arise from within 2 AU of the star. Schindhelm et al. (2012) found similar emission properties for a larger number of T Tauri stars: H₂ temperatures of 2500 ± 1000 K and $\log(N_{\text{H}_2}/\text{cm}^{-2}) = 19 \pm 1$. The UV fluorescent H₂ profiles reported by France et al. (2012) for non-transition T Tauri stars indicate that the emission arises from disk radii $\sim 0.1 - 1$ AU. To capture these properties of the H₂ emission, in Figure 6 we assume an H₂ temperature range of 1500–3500 K, an H₂ column density of $\log(N_{\text{H}_2}/\text{cm}^{-2}) = 18 - 20$, and that the bulk of the emission arises from within 0.7 AU.

CO Fundamental Emission:

Using LTE slab model fits to spectra of CO fundamental emission from classical T Tauri stars (CTTS), Najita et al. (2003) inferred that the emission is not optically thin, with typical temperatures 1100–1500 K and line-of-sight CO column densities $\sim 10^{18} \text{ cm}^{-2}$. Studying a different set of CTTS, Salyk et al. (2011b, see also 2011a) inferred similar rotational excitation temperatures of 1000–1700 K, line-of-sight CO column densities $10^{18} - 10^{19} \text{ cm}^{-2}$, and projected emitting areas πR_e^2 of 0.18–0.7 AU² (their Table 5) corresponding to $R_e \simeq 0.25 - 0.5$ AU. If we assume an average

deprojection correction factor of $\sqrt{2}$ for the emitting area, the equivalent $R_e \simeq 0.3 - 0.6$ AU. While much of the emission may arise within 0.6 AU, fitting the line profiles with Keplerian rotation models implies that the emission extends to larger radii, > 2 AU.

Similar conclusions were found by Banzatti & Pontoppidan (2015) and Bast et al. (2011). Banzatti & Pontoppidan (2015) decomposed the CO emission from CTTS into broad and narrow components. The shape of the broad component is fit as emission extending from $\sim 0.05 - 0.3$ AU, and the narrow component as emission from $\sim 0.5 - 2$ AU. In their study of the subset of CO emission sources with a single narrow peak and broad base ($\sim 15\%$ of all sources), Bast et al. (2011) inferred lower rotational temperatures of $\sim 300 - 800$ K; the lack of spatially extended emission constrained the origin of the emission to within a few AU of the central star. In Figure 6 we assume a CO temperature range (800–2000 K) that emphasizes the warmer range of reported values, a vertical CO column density $\log(N_{\text{CO}}/\text{cm}^{-2}) = 17.5 - 18.5$, and that the bulk of the emission arises from within 0.7 AU.

Spitzer Molecular Emission

Spectra taken with the *Spitzer Space Telescope* have been modeled with simple LTE slab models to characterize the detected molecular emission. The slab models (which are parameterized by a temperature, column density and emitting area for each molecular species) reproduce the spectra fairly well. In their study of the IRS SH emission from a modest sample of classical T Tauri stars, Carr & Najita (2011) reported best fitting water emission temperatures in a narrow range of values 575–650 K, water column densities $4 \times 10^{17} - 2 \times 10^{18} \text{ cm}^{-2}$, and projected emitting areas πR_e^2 with $R_e = 0.8 - 1.5$ AU based on fits to the emission at 12–16 μm . The HCN emission was found to be rotationally and vibrationally hot with temperatures 500–900 K, best fitting HCN column densities $2 \times 10^{16} - 6 \times 10^{16} \text{ cm}^{-2}$ corresponding to emission that is optically thick or marginally optically thick, and $R_e = 0.3 - 0.6$ AU. An optically thin fit is not excluded; if the HCN emission has an emitting area equal to that of the water emission from a given source, the HCN emitting column density is 10 times smaller than in the optically thick fit, i.e., with a column density $2 \times 10^{15} - 6 \times 10^{15} \text{ cm}^{-2}$.

The properties of the C_2H_2 and CO_2 emission are more weakly constrained. Assuming the C_2H_2 emission has the same temperature and emitting area as HCN, the C_2H_2 emitting column densities were found to be 0.04–0.4 that of HCN. The best-fitting CO_2 temperature was lower than for HCN, in the range 200–600 K assuming LTE, with the emission arising from an area corresponding to $R_e > 0.6 - 2$ AU, and the CO_2 column density unconstrained. The low inferred CO_2 temperature may reflect an origin in cooler gas (farther out or deeper in the atmosphere) than HCN, or possibly non-LTE level populations (Bosman et al. 2017).

Carr & Najita (2011) did not fit the OH emission in the IRS SH module with an LTE slab model. The OH emission from classical T Tauri stars at IRS SH wavelengths is non-thermal in origin, with a characteristic rotational temperature of ~ 4000 K, and likely arises from hot OH produced by the photodissociation of water (Najita et al. 2010; Carr & Najita 2011, 2014). In contrast, the lower rotational OH lines detected in the LH module probe rotationally cooler gas consistent with thermal

emission. Carr & Najita (2008) fit the LH OH emission from AA Tau, finding a temperature 575 K, an OH column density $9 \times 10^{16} \text{ cm}^{-2}$, and an emitting area corresponding to $R_e = 2.2 \text{ AU}$.

Complementing the above studies, Salyk et al. (2011a) modeled the Spitzer IRS spectra of a larger sample of stars with LTE slab models. To characterize the water emission, they fit 65 water features in the 10–35 μm range and inferred emission properties similar to those reported by Carr & Najita (2011): projected water emitting areas corresponding to $R_e = 0.8 - 2 \text{ AU}$, temperatures 400–800 K, and water column densities in the range $\log(N_{\text{H}_2\text{O}}/\text{cm}^{-2}) \simeq 17.6 - 19$ with a typical column density of $\log(N_{\text{H}_2\text{O}}/\text{cm}^{-2}) = 18$, where the ranges reflect the values found for individual CTTS.

The other molecules were assumed to have the same emitting area as water. With this assumption, the HCN emission is optically thin, with column densities in the range $\log(N_{\text{HCN}}/\text{cm}^{-2}) = 15 - 16$ and temperatures 600–800 K. The C_2H_2 is found to be warmer, with a temperature $T \sim 1000 \text{ K}$ and a column density 0.1 of HCN. A similar column density ratio was found by Carr & Najita (2011). The CO_2 emission allowed a range of temperatures 400–1000 K and $\log(N_{\text{CO}_2}/\text{cm}^{-2}) = 14.5 - 16$. The OH doublets in the 17–30.5 μm region were best fit with a warm temperature 900–1100 K and column densities in the range $\log(N_{\text{OH}}/\text{cm}^{-2}) \sim 15 - 16.3$. The NH_3 column density was constrained to $\log(N_{\text{NH}_3}/\text{cm}^{-2}) < 16$ for an assumed temperature of 400 K.

To capture these properties of the *Spitzer* molecular emission, in Figure 6 we assume a temperature range of 400–1000 K for water, HCN, CO_2 and NH_3 to span the range of reported values and their uncertainties. Because Salyk et al. (2011a) found higher temperatures for C_2H_2 and OH, we assume a slightly larger temperature range of 400–1500 K for C_2H_2 and a higher temperature range of 800–2000 K for OH. The range of observed water column densities is shown as an order of magnitude around the typical value of $\log(N_{\text{H}_2\text{O}}/\text{cm}^{-2}) = 18$. Typical column densities for HCN and CO_2 are shown as $\log(N/\text{cm}^{-2}) = 15 - 16$, with C_2H_2 an order of magnitude lower. The OH column density is shown as $\log(N_{\text{OH}}/\text{cm}^{-2}) = 15.3 - 16.5$. We also assume that the bulk of the emission from all of these species arises from within the typical water-emitting region, or $R_e = 1 \text{ AU}$.

References

- Ádámkóvics, M., Glassgold, A. E., & Meijerink, R. 2011, *ApJ*, 736, 143
- Ádámkóvics, M., Glassgold, A. E., & Najita, J. R. 2014, *ApJ*, 786, 135 (AGN14)
- Ádámkóvics, M., Najita, J. R. & Glassgold, A. E. 2016, *ApJ*, 817, 82 (ANG16)
- Akimkin, V., Zhukovska, S., Wiebe, D., et al. 2013, *ApJ*, 766, 8
- Bai, X. & Goodman, J. 2009, *ApJ*, 701, 737
- Bai, X. & Stone, J. M. 2013, *ApJ*, 769, 76
- Bai, X., Ye, J., Goodman, J., & Yuan, F. 2016, *ApJ*, 818, 152
- Balbus, S. A. & Hawley, J. F. 1992, *ApJ*, 400, 610
- Banzatti, A. & Pontoppidan, K. M. 2015, *ApJ*, 809, 167
- Bast, J. E., Brown, J. M., Herczeg, G. J., van Dishoeck, E. F., & Pontoppidan, K. M. 2011, *A&A*, 527
- Bergin, E., Calvet, N., D’Alessio, P., & Herczeg, G. J. 2003, *ApJL*, 591, L159
- Bethell, T., & Bergin, E. 2009, *Sci*, 326, 1675
- Bethell, T. J., & Bergin, E. A. 2011, *ApJ*, 739, 78
- Bosman, A., Bruderer, S., & van Dishoeck, E. F. 2017, arXiv:170108040
- Bruderer, S., Harsono, D., & van Dishoeck, E. F. 2015, *A&A*, 575, 94
- Carmona, A. 2010, *Earth, Moon, & Planets*, 106, 71
- Carr, J. S., Tokunaga, A. T., Najita, J., Shu, F. H., & Glassgold, A. E. 1993, *ApJ*, 411, L37
- Carr, J. S., Tokunaga, A. T., & Najita, J. 2004, *ApJ*, 603, 213
- Carr, J. S. & Najita, J. R. 2008, *Science*, 319, 1504
- Carr, J. S. & Najita, J. R. 2011, *ApJ*, 733, 102
- Carr, J. S. & Najita, J. R. 2014, *ApJ*, 788, 66
- Chiang, E. I. & Goldreich, P. 1997, *ApJ*, 490, 368
- D’Alessio, P., Calvet, N., Hartmann, L., Lizano, S., & Cantó, J. 1999, *ApJ*, 527, 893
- D’Alessio, P., Calvet, N., Hartmann, L., Franco-Hernández, R., & Servín H. 2006, *ApJ*, 638, 314
- D’Alessio, P., Calvet, N., Hartmann, L., Lizano, S., & Cantó, J. 1999, *ApJ*, 527, 893
- de Gregorio-Monsalvo, I., Ménard, F., Dent, W., et al. 2013, *AA*, 557, 133

- Doppmann, G. W., Najita, J. R., Carr, J. S., & Graham, J. R. 2011, *ApJ*, 738, 112
- Draine, B. T. & Bertoldi, F. 1996, *ApJ*, 468, 269
- Du, F., & Bergin, E. A. 2014, *ApJ*, 792, 2
- Ercolano, B., Clarke, C. J., & Drake, J. J. 2009, *ApJ*, 699, 1639
- Flaherty, K. M., Hughes, A. M., Rosenfeld, K. A., et al. 2015, *ApJ*, 813, 99
- France, K., Schindhelm, E., Herczeg, G. J., et al. 2012, *ApJ*, 756, 171
- Fraser, H. J., Collings, M. P., McCoustra, M. R. S., & Williams, D. A. 2001, *MNRAS*, 327, 1165
- Furlan, E., Calvet, N., D'Alessio, P., et al. 2005, *ApJ*, 628, 65
- Gammie, C. 1996, *ApJ*, 457, 355
- Glassgold, A. E., Meijerink, R., & Najita, J. R. 2009, *ApJ*, 701, 142
- Glassgold, A. E., & Najita, J. R. 2001, in *ASP Conf. Ser. 244, Young Stars Near Earth: Progress and Prospects*, ed. R. Jayawardhana & T. Greene (San Francisco, CA: ASP), 251
- Glassgold, A. E., Najita, J., & Igea, J. 2004, *ApJ*, 615, 972 (GNI04)
- Glassgold, A. E., & Najita, J. R. 2015, *ApJ*, 810, 125
- Gorti, U., & Hollenbach, D. 2008, *ApJ*, 683, 287
- Gressel, O., Turner, N. J., Nelson, R. P. & McNally, C. P. 2015, *ApJ*, 801, 84
- Guilloteau, S., Dutrey, A., Wakelam, V., et al. 2012, *A&A*, 548, 70
- Hartmann, L., Calvet, N., Gullgring, E., & D'Alessio, P. 1998, *ApJ*, 495, 385
- Heinzeller, D., Nomura, H., Walsh, C., & Millar, T. J. 2011, *ApJ*, 731, 115
- Herczeg, G. J., Wood, B. E., Linsky, J. L., Valenti, J. A., & Johns-Krull, C. M. 2004, *ApJ*, 607, 369
- Hirose, S. & Turner, N. J. 2011, *ApJ*, 732, L30
- Hughes, A. M., Wilner, D. J., Andrews, S. M., et al. 2011, *ApJ*, 727, 85
- Jonkheid, B., Faas, F. G. A., van Zadelhoff, G.-J., & van Dishoeck, E. F. 2004, *AA*, 428, 511
- Kamp, I., & Dullemond, C. P. 2004, *ApJ*, 615, 991
- Kamp, I., & van Zadelhoff, G.-J. 2001, *A&A*, 373, 641
- Kunz, M. W. & Lesur, G. 2013, *MNRAS*, 434, 2295
- Lesur, G., Kunz, M. W., & Fromang, S. 2014, *A&A*, 566, 56

- Li, X., Heays, A. N., Visser, R., et al. 2013, *A&A*, 555, A14
- Meeus, G., Salyk, C., Bruderer, S., Fedele, D., Maaskant, K., Evans, N. J. II, van Dishoeck, E. F. 2013, *AA*, 559, 84
- Meijerink, R., Pontoppidan, K. M., Blake, G. A., Poelman, D. R., & Dullemond, C. P. 2009, *ApJ*, 704, 1471
- Najita, J., Carr, J. S., Glassgold, A. E., & Valenti, J. A. 2007, in *Protostars and Planets V*, ed. B. Reipurth, D. Jewitt, & K. Keil (Tucson: Univ. Arizona Press), 507
- Najita, J., Carr, J. S., Glassgold, A. E., Shu, F. H., & Tokunaga, A. T. 1996, *ApJ*, 456, 292
- Najita, J., Carr, J. S., & Mathieu, R. D. 2003, *ApJ*, 589, 931
- Najita, J. R., Ádámkóvics, M., & Glassgold, A. E. 2011, *ApJ*, 743, 147
- Najita, J. R., Doppmann, G. W., Carr, J. S., Graham, J. R., & Eisner, J. A. 2009, *ApJ*, 691, 738
- Najita, J. R., Carr, J. S., Strom, S. E., Watson, D. M., Pascucci, I., Hollenbach, D., Gorti, U., & Keller, L. 2010, *ApJ*, 712, 274
- Nomura, H., Aikawa, Y., Tsujimoto, M., Nakagawa, Y., & Millar, T. J. 2007, *ApJ*, 661, 334
- Öberg, K. I., Linnartz, H., Visser, R., & van Dishoeck, E. F., 2009, *ApJ*, 693, 1209
- Palla, F., Salpeter, E. E., Stahler, S. W. 1983, *ApJ*, 271, 632
- Pontoppidan, K. M., Salyk, C., Blake, G. A., Meijerink, R., Carr, J. S., & Najita, J. 2010, *ApJ*, 720, 887
- Rab, C., Baldovin-Saavedra, C., Dionatos, O., Vorobyov, E., & Güdel, M. 2016, *SSR*, 205, 3
- Salyk, C., Blake, G. A., Boogert, A. C. A., & Brown, J. M. 2009, *ApJ*, 699, 330
- Salyk, C., Pontoppidan, K. M., Blake, G. A., Najita, J. R., & Carr, J. S. 2011a, *ApJ*, 731, 130
- Salyk, C., Blake, G. A., Boogert, A. C. A., & Brown, J. M. 2011b, *ApJ*, 743, 112
- Schindhelm, E., France, K., Herczeg, G. J., et al. 2012, *ApJ*, 756, L23
- Simon, M., Pascucci, I., Edwards, S., et al. 2016, *ApJ*, 831, 169
- Teague, R., Guilloteau, S., Semenov, D., et al. 2016, *A&A*, 592, 49
- Thi, W.-F. & Bik, A. 2005, *A&A*, 557, 570
- Turner, N. J., Fromang, S., Gammie, C., et al. 2014, in *Protostars and Planets VI*, ed. H. Beuther et al. (Tucson, AZ: Univ. of Arizona Press), 411
- Visser, R., van Dishoeck, E. F., & Black, J. H. 2009, *A&A*, 503, 323

Walsh, C., Nomura, H., Millar, T. J., & Aikawa, Y. 2012, *ApJ*, 747, 114

Woitke, P., Kamp, I., & Thi, W.-F. 2009, *A&A*, 501, 383

Wolk, S. J., Harnden, F. R., Flaccomio, E., Micela, G., Favata, F., Shang, H., & Feigelson, E. D. 2005, *ApJSS*, 160, 423

Woods, P. M., & Willacy, K. 2009, *ApJ*, 693, 1360

Yang, H., Herczeg, G. J., Linsky, J. L., et al. 2012, *ApJ*, 744, 121

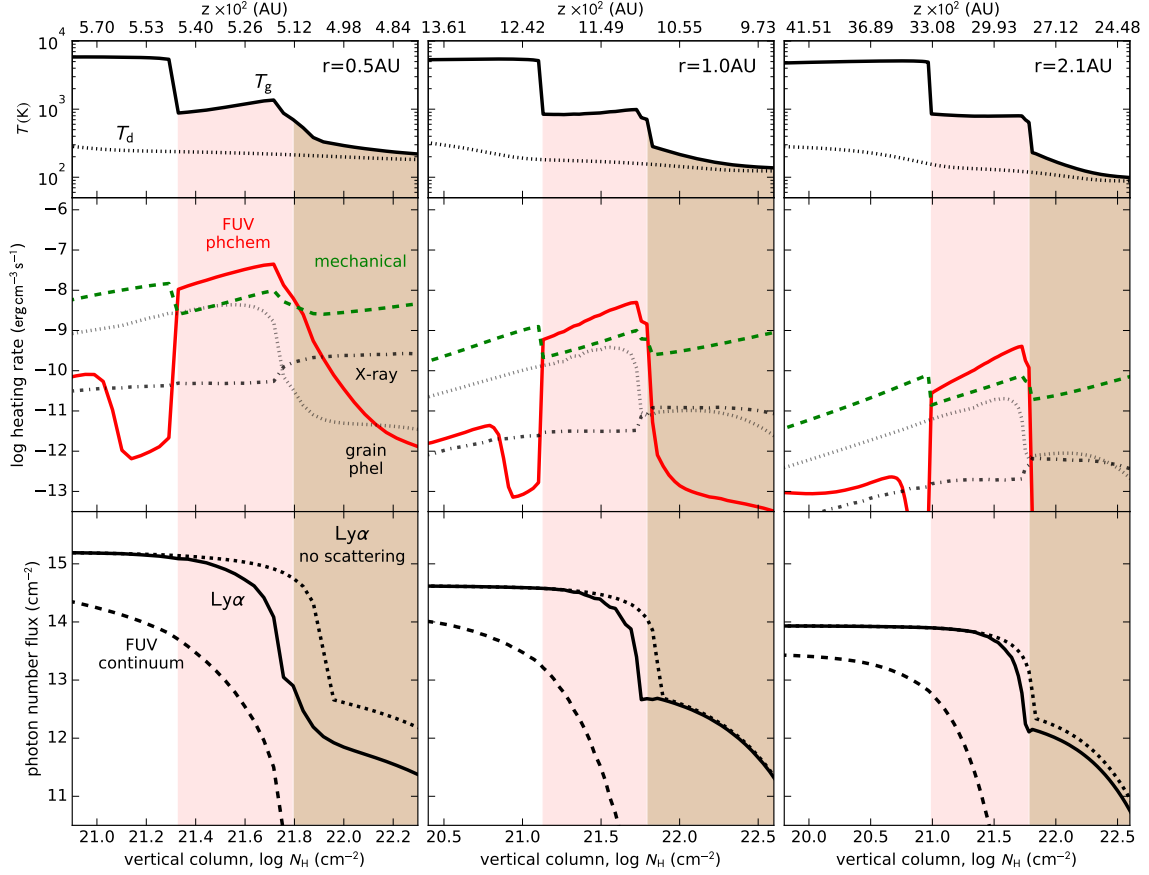


Fig. 7.— Extension of Fig. 1 to 2 AU. Vertical profiles of gas and dust temperatures (top row of panels, solid and dotted lines, respectively), heating rates (middle row) and FUV radiation fields (bottom row) at 0.5 AU, 1.0 AU, and 2.1 AU (panels in left, center and right columns, respectively) in our reference model. FUV photochemical heating (red solid line) dominates in the warm upper molecular layer of the disk (strawberry shading) where the FUV continuum and Ly α are absorbed. Mechanical heating (green dashed line) dominates above and below this region. X-ray (dash-dotted line) and grain photoelectric heating (dotted line) are shown for comparison. The FUV continuum and Ly α are strongly attenuated in the photochemically-heated layer.

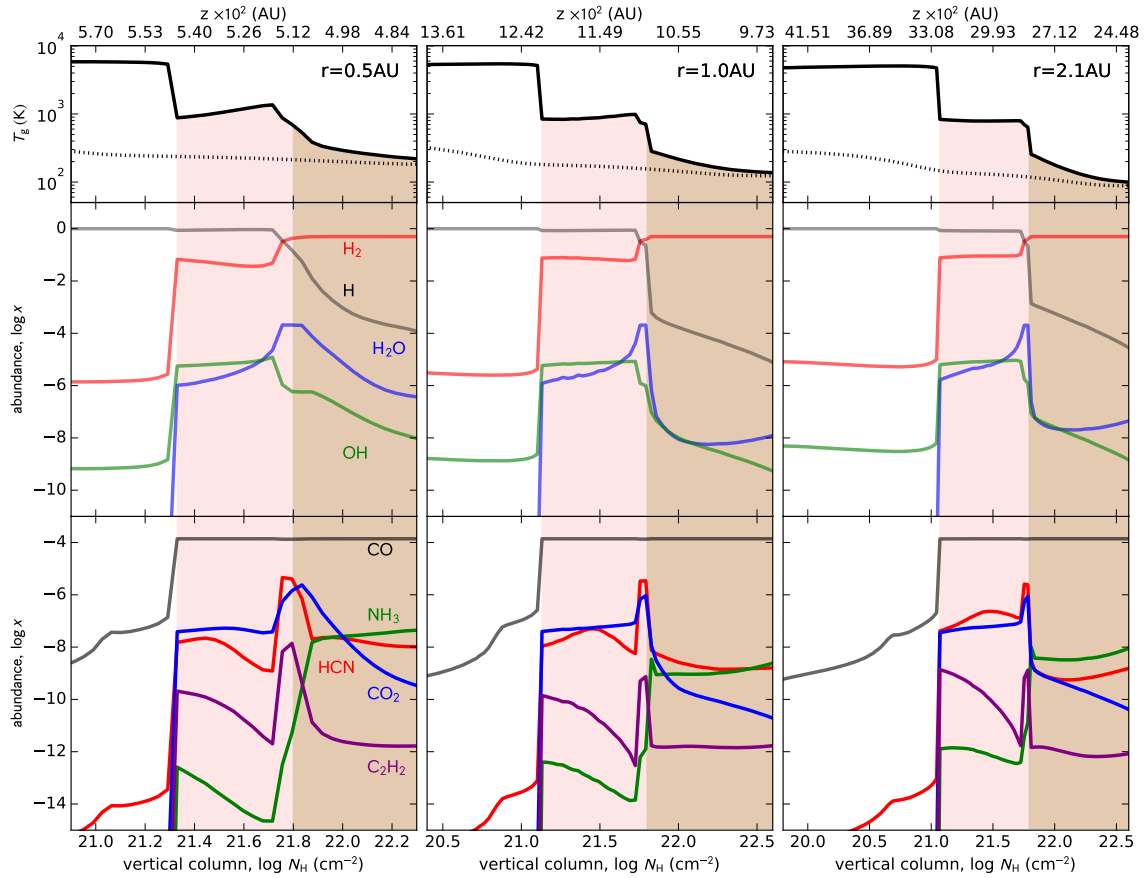


Fig. 8.— Extension of Fig. 2 to 2 AU. Vertical profiles of temperatures (top row of panels) and abundances (middle and bottom row) at 0.5 AU, 1.0 AU, and 2.1 AU (panels in left, center and right columns, respectively) for our reference model. The warm upper layer where FUV heating dominates (strawberry shading) is rich in molecular species that are commonly detected from T Tauri disks. The cooler mechanically heated layer (chocolate shading) lies below.

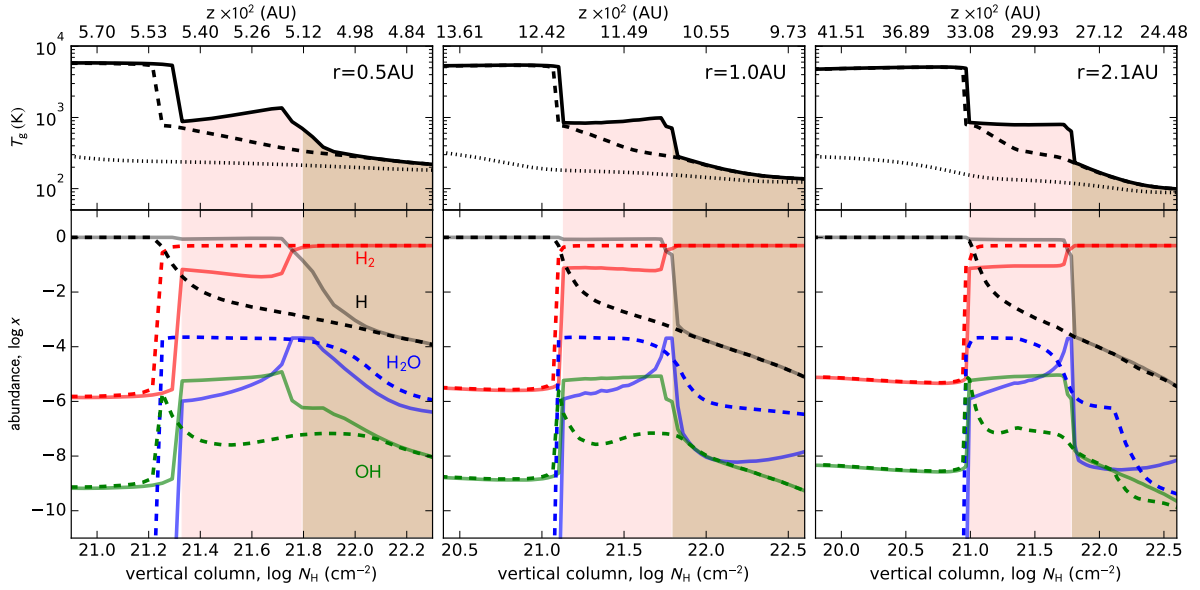


Fig. 9.— Extension of Fig. 3 to 2 AU. Vertical profiles of gas temperatures (top row of panels) and molecular abundances (bottom panels) with and without Ly α irradiation (solid and dashed lines respectively) at 0.5AU, 1.0, and 2.1AU (panels in left, center and right columns, respectively). When Ly α is not present, the molecular portion of the atmosphere is cooler, and the molecular transition occurs higher in the atmosphere. When present, Ly α dissociates H₂O and enhances the OH abundance in both the FUV-heated (strawberry shading) and mechanically-heated (chocolate shading) layers.

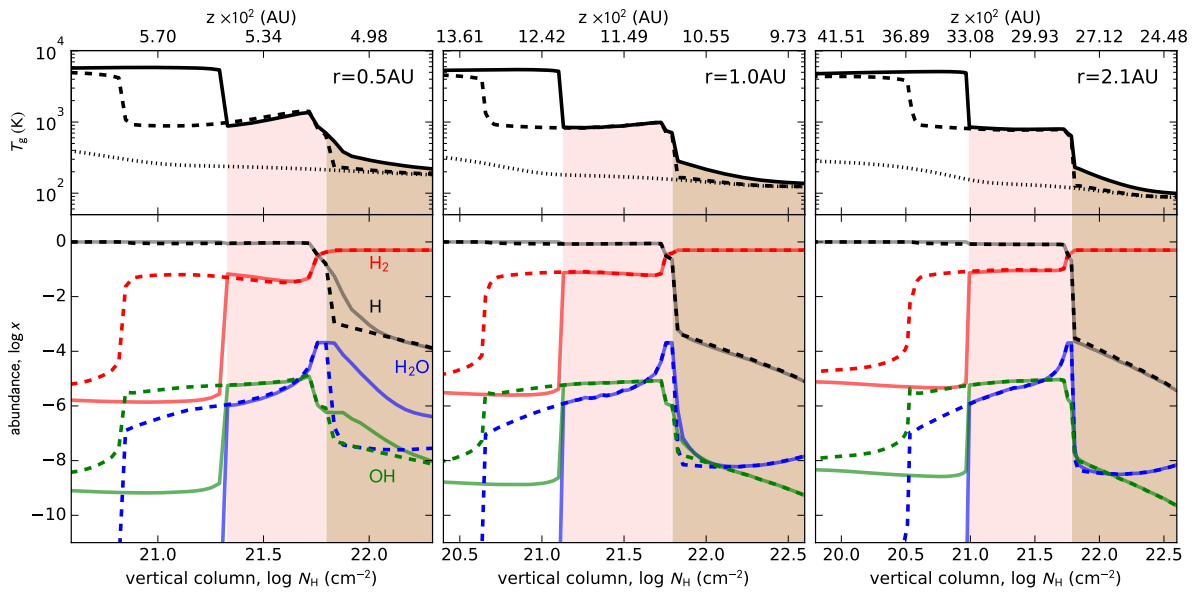


Fig. 10.— Extension of Fig. 4 to 2 AU. Vertical profiles of gas temperature (top row of panels) and molecular abundances (bottom panels) with and without mechanical heating (solid and dashed lines, respectively) at 0.5 AU, 1.0 AU, and 2.1 AU (panels in left, center and right columns, respectively). In models with reduced mechanical heating, the molecular transition occurs higher in the atmosphere and the temperature is reduced in the molecular region below the FUV-heated layer.